PROCEEDINGS OF SCIENCE

Implications of late-time XRT detected GRBs for particle acceleration

Zhi-Qiu Huang,[a,*] **Annalisa Celotti,**[a] **Om Sharan Salafia,**[b] **Lara Nava**[b] **and Giancarlo Ghirlanda**[b]

[a] *SISSA,*
Via Bonomea 265, 34136 Trieste, Italy
[b] *INAF, Osservatorio Astronomico di Brera,*
Via E. Bianchi, 46, 23807 Merate, Italy
E-mail: zhhuang@sissa.it, celotti@sissa.it, om.salafia@inaf.it, lara.nava@inaf.it, giancarlo.ghirlanda@inaf.it

Relativistic shocks have been widely studied as promising sites for ultra-high-energy particle acceleration. Predictive results have been obtained from both analytical and numerical methods but require tests from observations. The gamma-ray burst (GRB) multi-wavelength 'afterglow' emission is believed to be produced in relativistic shocks where high-energy electrons are accelerated. Afterglow observations thus provide information to test our current understanding of shock acceleration. Here we focus on six GRBs with determined redshifts, selected for having XRT afterglow detection at $\sim 10^7$ seconds after the GRB trigger time. We show that these observations lead to meaningful constraints on the maximum electron energy in the underlying shocks.

39th International Cosmic Ray Conference (ICRC2025)
15–24 July 2025
Geneva, Switzerland

ICRC 2025
The Astroparticle Physics Conference
Geneva July 15-24, 2025

*Speaker

PoS(ICRC2025)050

1. Introduction

Gamma-ray bursts (GRBs), especially in the 'afterglow' phase [e.g. 1–3], have been well studied thanks to abundant observations. The afterglow emission is widely accepted to be produced by high-energy electrons accelerated at external shocks, and hence contains information on particle acceleration at relativistic shocks.

Numerical simulations demonstrate that weakly-magnetized relativistic shocks, as in the GRB afterglow case, are mediated by the Weibel instability. Particles can be scattered by the triggered small scale turbulence and keep crossing the shock front to gain energy. The process is expected to produce electrons with a power-law energy distribution up to some maximum energy, but the process governing the maximum energy is not yet well understood. Observations of GRB afterglows could provide crucial constraints.

Simulations dedicated to study particle acceleration at GRB external shocks found that the maximum accelerated energy decreases with time [4]. When the synchrotron frequency associated to such maximum energy is located within the energy band accessible by X-ray telescopes, this could produce some detectable features.

In this work, we study how the X-ray synchrotron emission from a relativistic blastwave observed at 10^6-10^7 s is contributed by parts of the equal-arrival-time surface (EATS) located at different latitudes. We find that the maximum synchrotron photon energy emitted by accelerated electrons is most likely to be located within the XRT energy band between 10^6 and 10^7 seconds, and hence a cutoff in the XRT spectra is expected theoretically.

We select several GRBs with XRT detections at times later than 10^7 s and analyze their spectra, downloaded from the *Swift* XRT catalog [5–7]. There is no convincing evidence of a cutoff in the XRT energy band, which provides constraints on the typical afterglow parameters. Here we present some preliminary results of the work which will be the subject of a paper in preparation.

2. Maximum Synchrotron Photon Energy

We consider two candidate mechanisms that can determine the maximum electron energy in shock acceleration. When synchrotron cooling balances acceleration, electrons cannot gain energy anymore and reach the cooling (or 'burnoff') limiting Lorenz factor $\gamma_{\rm syn}$. If a relativistic blast wave is observed at a time $t_{\rm obs}$ after the explosion, these electrons emit at a typical synchrotron photon energy $h\nu_{\rm syn}$ given by[1] [4]

$$h\nu_{\rm syn} \simeq \begin{cases} 1.49 E_{\rm k,54}^{1/4} n_0^{-1/12} \epsilon_{\rm B,-2}^{-1/6} (1+z)^{-1/4} t_{\rm obs,2}^{-3/4}\,{\rm GeV}, & {\rm ISM} \\ 0.91 E_{\rm k,54}^{1/3} A_\star^{-1/6} \epsilon_{\rm B,-2}^{-1/6} (1+z)^{-1/3} t_{\rm obs,2}^{-2/3}\,{\rm GeV}, & {\rm wind} \end{cases} \quad (1)$$

where $E_{\rm k}$ is the isotropic-equivalent shock energy and $\epsilon_{\rm B}$ is the fraction of the shock energy that is carried by the downstream turbulent magnetic field. Here 'ISM' stands for interstellar medium (i.e. a scenario where the medium into which the shock propagates has a uniform number density n), while 'wind' indicates a wind-like stratified medium (with a number density $n(R) = AR^{-2}$, where R is the radial distance from the progenitor).

[1] We adopt the notation $Q_x = Q_{\rm cgs}/10^x$, where Q is any quantity and $Q_{\rm cgs}$ is its value expressed in cgs units.

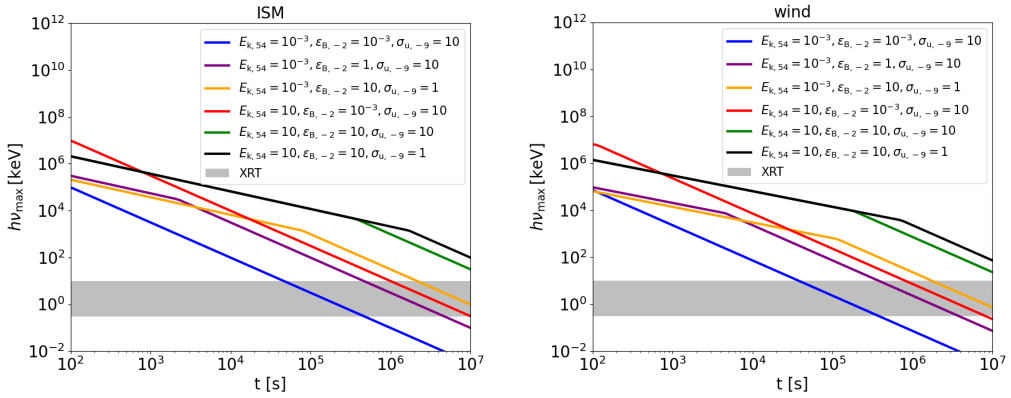

Figure 1: Maximum synchrotron photon energy $h\nu_{\rm max} = \min\left[h\nu_{\rm syn}, h\nu_{\rm sat}\right]$ adopting several sets of parameters. The redshift is fixed to $z = 0.2$. The gray area represents the XRT energy band.

Besides, the acceleration process can be quenched when the isotropization rate in the downstream frame becomes smaller than the gyrofrequency, in which case downstream particles are constrained to move along the magnetic lines parallel to the shock and can hardly cross the shock. This happens when the particle energy exceeds the so-called 'saturation' or 'magnetized' limit $\gamma_{\rm sat}$, with the corresponding observed synchrotron photon energy [4]

$$h\nu_{\rm sat} \simeq \begin{cases} 285 E_{\rm k,54}^{1/2} \epsilon_{\rm B,-2}^{1/2} \sigma_{\rm u,-9}^{-1/2} (1+z)^{1/2} t_{\rm obs,2}^{-3/2}\,{\rm GeV}, & {\rm ISM} \\ 209 E_{\rm k,54}^{1/2} \epsilon_{\rm B,-2}^{1/2} \sigma_{\rm u,-9}^{-1/2} (1+z)^{1/2} t_{\rm obs,2}^{-3/2}\,{\rm GeV}, & {\rm wind} \end{cases} \tag{2}$$

where $\sigma_{\rm u}$ is the upstream magnetization parameter. We plot the maximum photon energy $h\nu_{\rm max} = \min\left[h\nu_{\rm syn}, h\nu_{\rm sat}\right]$ in Fig. 1.

For typical afterglow parameters, the maximum synchrotron photon energy at $t \geqslant 10^6$ s $h\nu_{\rm max}$ should be fixed by $h\nu_{\rm sat}$ and should cross the XRT energy band soon after, which would result in some observational features, such as a cutoff in the spectra.

3. High latitude emission

For an extended source expanding at relativistic speed, photons received by an observer at the same time are emitted at different times in the lab frame. If the shock is approximated by an infinitely thin surface, then the locus of emission locations that correspond to the same arrival time is itself a surface, and it is usually referred to as the EATS.

Following Sari [8], photons emitted at a latitudinal angle θ from the line of sight can be detected by the observer at time

$$t_{\rm obs} = (1+z)\,(t - R\cos\theta/c)\,, \tag{3}$$

where t is the emission time in the lab frame, measured since the explosion.

Assuming an isotropically propagating shock, the relation between R and t is independent of θ. We have [9],

$$R = ct/\left[1 + \frac{1+z}{2(4-k)\Gamma_{\rm sh}^2}\right]. \tag{4}$$

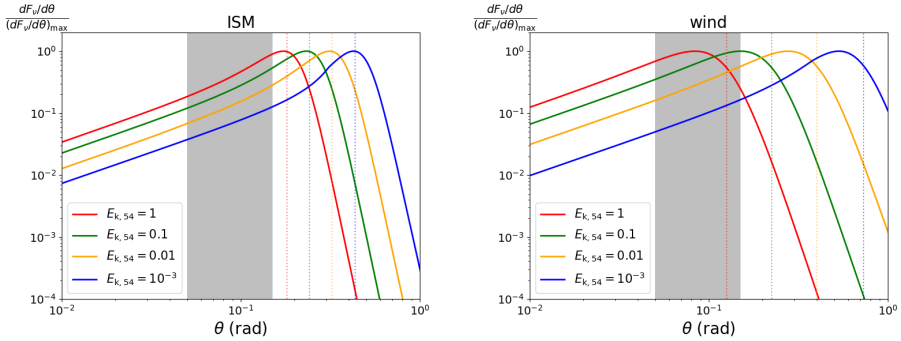

Figure 2: $dF_\nu/d\theta$ from different latitudes at $t = 3 \times 10^6$ s adopting $p = 2.2$ and $z = 0.2$. Left panel: ISM case with $n_0 = 1$. Right panel: wind case with $A_\star = 1\,\mathrm{cm}^{-1}$.

Inserting Eq. 4 into Eq. 3, photons that are observed at $t_{\rm obs}$ and coming from the latitudinal angle θ, are emitted at the radius $R_{\rm obs}$ given b

$$R_{\rm obs}(\theta, t_{\rm obs}) = \frac{ct_{\rm obs}}{1 - \cos\theta + (1+z)/2(4-k)\Gamma^2_{\rm sh}(R_{\rm obs})}. \tag{5}$$

The total observed flux density is obtained by integrating over the EATS, Eq. 5, namely

$$F_\nu = \frac{1}{2}\int \mathcal{D}^2 F_{\nu,\rm max}(R_{\rm obs}) f(\nu/\mathcal{D}) \sin\theta d\theta. \tag{6}$$

Here $F_{\nu,\rm max} \equiv \mathcal{D} N_{\rm e} P'_{\nu,\rm max}/4\pi D_{\rm L}^2$, here $D_{\rm L}$ is the luminosity distance. The peak of a single-electron synchrotron spectral power is $P'_{\nu,\rm max} = \sigma_{\rm T} m_{\rm e} c^2 B/3e$. Here $f(\nu')$ encodes the various power regimes in the slow cooling case.

In Fig. 2 we plot $dF_\nu/d\theta$ at $\nu/\mathcal{D} > \nu'_c$ from different latitudinal angles, assuming $\nu'_{\rm max}$ to be infinity. High energy emissions are mainly contributed by regions with latitudinal angles around $\theta_{\rm c}$, where $\theta_{\rm c}$ is the critical angle where the angular differential flux $dF_\nu/d\theta$ reaches its maximum. $\theta_{\rm c}$ is derived by numerically solving $\theta_{\rm c} = \sin^{-1}[\frac{1}{\Gamma(R_{\rm obs})}]$ with Eq.5. It is shown by the dashed vertical lines in Fig. 2.

Note that the critical angle $\theta_{\rm c}$ is related to the Lorentz factor of the shock. $\theta_{\rm c}$ would increase with time as the shock decelerates. Because of the collimation of the GRB ejecta, the blast wave shock is not spherical. In the simplest description, it can be assumed to feature a border whose angular separation from the symmetry axis is given by the jet opening angle $\theta_{\rm j}$. It is possible that $\theta_{\rm j} < \theta_{\rm c}$ at late times, in which case high-energy photons are mainly contributed from the edge of the shock rather than from the critical angle. The gray area represents the typical range of the jet opening angle $\theta_{\rm j} within [0.05, 0.15]$ radians [11]. For typical parameters, $\theta_{\rm j} \lesssim \theta_{\rm c}$ can be satisfied at quite late times.

4. Parameter space for $h\nu_{\rm max}$

The upstream magnetization parameter $\sigma_{\rm u}$ is defined as

$$\sigma_{\rm u} = \frac{B_{\rm u}^2}{4\pi n m_{\rm p} c^2}. \tag{7}$$

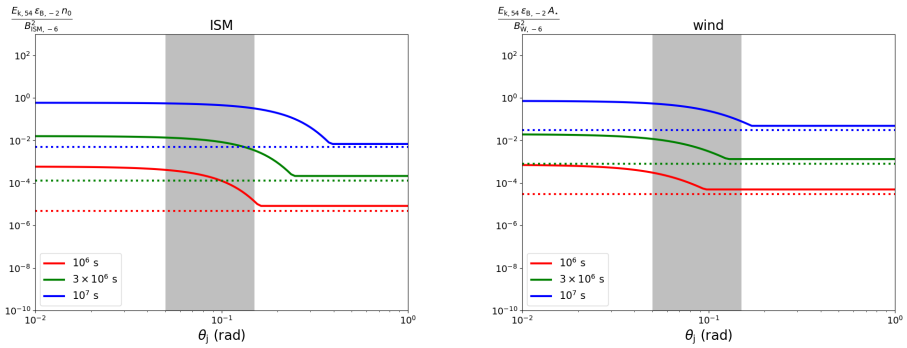

Figure 3: Parameter space for the case in which $h\nu_{\rm max} = 3$ keV at 10^6, 3×10^6 and 10^7 s. $z = 0.2$ is adopted. The gray shaded area corresponds to $\theta_{\rm jet} within [0.05, 0.15]$ rad. We fix $E_{\rm k,54}/n_0 = 1$ in the left panel and $E_{\rm k,54}/A_\star = 1$ in the right-hand panel. The solid curves represent the results from this work and the dotted ones represent those from Sironi et al. [4].

We use the strength of the upstream magnetic field $B_{\rm u}$ and the number density n to replace $\sigma_{\rm u}$. In the wind case, we assume the magnetic field in the stellar wind to be toroidal and to evolve with the radius R as $B \propto R^{-1}$. Hence, $\sigma_{\rm u}$ is constant. Following Sagi & Nakar [12], we consider $B_{\rm W}$ and n at $R = 10^{18}$ cm.

As shown in Fig. 2, when $\theta_{\rm j} < \theta_{\rm c}$ most high energy emission comes from the edge of the jet. While when $\theta_{\rm j} > \theta_{\rm c}$, high energy photons are mainly emitted around $\theta_{\rm c}$.

In Fig. 3, we consider the maximum photon energy from min[$\theta_{\rm j}$,$\theta_{\rm c}$] and show the parameter space for $h\nu_{\rm max} = 3$ keV. The dashed lines represent the results for from Eq. 2, and the shaded area represents the space for typical values of the parameters. With the evidence of the cutoff energy at late-time spectra, we can get more realistic constraints on the parameter space.

5. Constraints from observations

We select six GRBs with XRT detections later than 10^7 s as well as redshift information, namely GRB 130427A, GRB 130702A, GRB 130925A, GRB 161219B, GRB 190829A and GRB221009A. For each event, we download spectral data in different time intervals from the *Swift* XRT catalog[5, 6]. With the X-ray data analysis tool *Xspec* [13], we fit the spectra in different periods with the model combination - TBABS × ZTBABS × (CFLUX × CUTOFFPL). The parameters of the models are listed in Tab. 1.

On the basis of our analysis, there is no evidence for a cutoff in the spectra. Hence we adopt the lower limit on the cutoff energy at the 2σ confidence level to constrain the parameter space. By combining the fitting results from all of the six GRBs, we plot in Fig. 4 the observational constraints on the parameter space, considering the lower limit of $E_{\rm cut}$ within 2 σ confidence. The curves represent the lower boundaries of the 'permitted' parameter space.

Model	Parameter
tbabs	$N_{\rm H}$ ($\times 10^{22}$ cm^{-2})
ztbabs	z
	$N_{\rm H}$ ($\times 10^{22}$ cm^{-2})
cflux	$E_{\rm min}$ = 0.3 keV
	$E_{\rm max}$ = 10 keV
	$\log_{10}$ Flux (erg cm^{-2} s^{-1})
cutofflog	Photon Index
	$\log(E_{\rm cut}/{\rm keV})$

Table 1: Parameters of the model TBABS × ZTBABS × (CFLUX × CUTOFFPL) that we use for the data fitting.

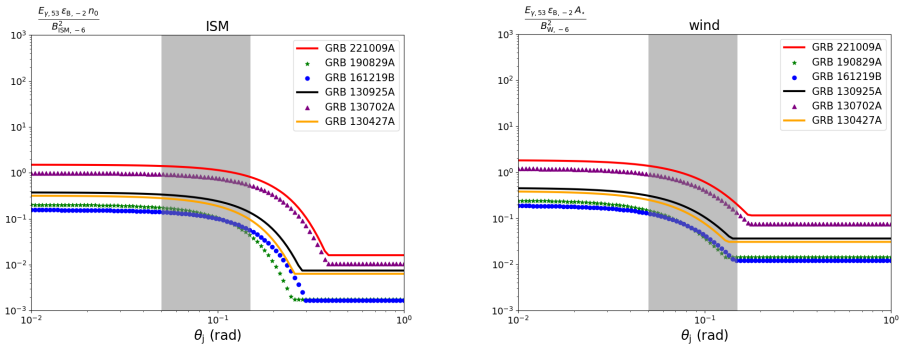

Figure 4: Constraints on the parameter space from six selected GRBs. Three GRBs that cannot satisfy the requirements on E_γ are labeled by special patterns: GRB 190829A with ⋆, GRB 161219B with • and GRB 130702A with ▲.

6. Conclusions

Based on recent numerical simulations, the maximum synchrotron photon energy should be located within the XRT energy band at around 10^7 s. In this work we focus on six GRBs with late-time XRT detections to set observational limits on the cutoff energy and hence on the maximum electron energy of the emitting electrons.

We find that there is no clear evidence of a cutoff. The lower limit on $E_{\rm cut}$ at the 2 σ confidence level provides constraints on the physical parameter space. Adopting typical values of the ambient number density $n_0/A_\star \sim 1$ and the upstream magnetic field $B_{\rm ISM/W,-6} \sim 1$ (here $B_{\rm ISM}$ is the constant magnetic field in the ISM case and $B_{\rm W}$ is the magnetic field in the wind case at $R = 10^{18}$ cm), we limit the values of $E_{\rm k,54} \gtrsim 1$ and $\epsilon_{\rm B,-2} \gtrsim 1$ for the selected GRB events.

Previous works considered the relation between the kinetic shock energy and the radiative prompt emission [14, 15]. The so-called radiative efficiency is defined as [14, 16]

$$\eta_\gamma = \frac{E_\gamma}{E_\gamma + E_{\rm k}}, \tag{8}$$

where E_γ is the isotropic gamma-ray energy emitted during the prompt phase. The typical value of

η_γ is $\sim 10\%$ [17–20], and could be larger in some specific GRBs [16, 21].

For GRB 130702A, GRB 161219B and GRB 190829A, $E_\gamma < 10^{51}$ erg [22–24]. Adopting $\eta_\gamma = 0.1$, the shock kinetic energies of these events can hardly satisfy the constraints from the late-time XRT observations. This in turn would require a more efficient acceleration process for the electrons to achieve a maximum energy higher than what predicticted by Sironi et al. [4]. The maximum accelerated electron energy should be much larger than what we expect from Sironi et al. [4]. Other instruments (i.e., NuSTAR) by detecting photons with energy larger than 10 keV at late times may provide more strict constraints on the parameter space and a better test on our current knowledge on particle acceleration.

Acknowledgements

This study was funded by the European Union - NextGenerationEU, in the framework of the PRIN Project "PEACE: Powerful Emission and Acceleration in the most powerful Cosmic Explosion" (code 202298J7KT– CUP G53D23000880006). The views and opinions expressed are solely those of the authors and do not necessarily reflect those of the European Union, nor can the European Union be held responsible for them. We acknowledge financial support from an INAF Mini Grant 2022 (PI L. Nava). This work made use of data supplied by the UK Swift Science Data Centre at the University of Leicester.

References

[1] Paczynski, B. 1997, , astro-ph/9712123. doi:10.48550/arXiv.astro-ph/9712123

[2] Costa, E., Frontera, F., Heise, J., et al. 1997, Nature, 387, 6635, 783. doi:10.1038/42885

[3] Chiang, J. & Dermer, C. D. 1999, The Astrophysical Journal, 512, 2, 699. doi:10.1086/306789

[4] Sironi, L., Spitkovsky, A., & Arons, J. 2013, The Astrophysical Journal, 771, 1, 54. doi:10.1088/0004-637X/771/1/54

[5] Evans, P. A., Beardmore, A. P., Page, K. L., et al. 2007, Astronomy and Astrophysics, 469, 1, 379. doi:10.1051/0004-6361:20077530

[6] Evans, P. A., Beardmore, A. P., Page, K. L., et al. 2009, Mon. Not. R. Astron. Soc., 397, 3, 1177. doi:10.1111/j.1365-2966.2009.14913.x

[7] Evans, P. A., Page, K. L., Beardmore, A. P., et al. 2023, Mon. Not. R. Astron. Soc., 518, 1, 174. doi:10.1093/mnras/stac2937

[8] Sari, R. 1998, The Astrophysical Journal Letter, 494, 1, L49. doi:10.1086/311160

[9] Blandford, R. D. & McKee, C. F. 1976, Physics of Fluids, 19, 1130. doi:10.1063/1.861619

[10] Huang, Z.-Q., Kirk, J. G., Giacinti, G., et al. 2022, The Astrophysical Journal, 925, 2, 182. doi:10.3847/1538-4357/ac3f38

[11] Fong, W., Berger, E., Metzger, B. D., et al. 2014, The Astrophysical Journal, 780, 2, 118. doi:10.1088/0004-637X/780/2/118

[12] Sagi, E. & Nakar, E. 2012, The Astrophysical Journal, 749, 1, 80. doi:10.1088/0004-637X/749/1/80

[13] Arnaud, K. A. 1996, Astronomical Data Analysis Software and Systems V, 101, 17.

[14] Zhang, B., Liang, E., Page, K. L., et al. 2007, The Astrophysical Journal, 655, 2, 989. doi:10.1086/510110

[15] Wang, X.-G., Zhang, B., Liang, E.-W., et al. 2015, The Astrophysical Journal Supplement, 219, 1, 9. doi:10.1088/0067-0049/219/1/9

[16] Lloyd-Ronning, N. M. & Zhang, B. 2004, The Astrophysical Journal, 613, 1, 477. doi:10.1086/423026

[17] Du, S., Lü, H.-J., Zhong, S.-Q., et al. 2016, Mon. Not. R. Astron. Soc., 462, 3, 2990. doi:10.1093/mnras/stw1869

[18] Hascoët, R., Daigne, F., & Mochkovitch, R. 2014, Mon. Not. R. Astron. Soc., 442, 1, 20. doi:10.1093/mnras/stu750

[19] Li, L., Wu, X.-F., Lei, W.-H., et al. 2018, The Astrophysical Journal Supplement, 236, 2, 26. doi:10.3847/1538-4365/aabaf3

[20] D'Avanzo, P., Salvaterra, R., Sbarufatti, B., et al. 2012, Mon. Not. R. Astron. Soc., 425, 1, 506. doi:10.1111/j.1365-2966.2012.21489.x

[21] Li, L. & Wang, Y. 2024, The Astrophysical Journal, 972, 2, 195. doi:10.3847/1538-4357/ad2511

[22] Golenetskii, S., Aptekar, R., Pal'Shin, V., et al. 2013, GRB Coordinates Network, Circular Service, No. 14986, #1 (2013), 14986, 1.

[23] Frederiks, D., Golenetskii, S., Aptekar, R., et al. 2016, GRB Coordinates Network, Circular Service, No. 20323, #1 (2016), 20323, 1.

[24] Tsvetkova, A., Golenetskii, S., Aptekar, R., et al. 2019, GRB Coordinates Network, Circular Service, No. 25660, 25660, 1.